



HAL
open science

Mo₄Ce₄Al₇C₃: A nanolamellar ferromagnetic Kondo lattice

Maxime Barbier, Fabrice Wilhelm, Damir Pinek, Kanji Furuta, Takahiro Ito, Youngsoo Kim, Maëlys Magnier, Daniel Braithwaite, Michal Vališka, Christine Opagiste, et al.

► **To cite this version:**

Maxime Barbier, Fabrice Wilhelm, Damir Pinek, Kanji Furuta, Takahiro Ito, et al.. Mo₄Ce₄Al₇C₃: A nanolamellar ferromagnetic Kondo lattice. *Physical Review B*, 2020, 102 (15), pp.155121. 10.1103/PhysRevB.102.155121 . hal-02994836

HAL Id: hal-02994836

<https://hal.science/hal-02994836>

Submitted on 31 May 2023

HAL is a multi-disciplinary open access archive for the deposit and dissemination of scientific research documents, whether they are published or not. The documents may come from teaching and research institutions in France or abroad, or from public or private research centers.

L'archive ouverte pluridisciplinaire **HAL**, est destinée au dépôt et à la diffusion de documents scientifiques de niveau recherche, publiés ou non, émanant des établissements d'enseignement et de recherche français ou étrangers, des laboratoires publics ou privés.

Mo₄Ce₄Al₇C₃: A nanolamellar ferromagnetic Kondo lattice

Maxime Barbier ^{1,2,*}, Fabrice Wilhelm,² Damir Pinek ¹, Kanji Furuta ³, Takahiro Ito ^{3,4}, Youngsoo Kim,⁵ Maëlys Magnier,⁵ Daniel Braithwaite ⁵, Michal Vališka ⁵, Christine Opagiste ⁶, Michel W. Barsoum,⁷ Philippe Ohresser,⁸ Edwige Otero,⁸ Patrick Le Fèvre,⁸ François Bertran ⁸, Gaston Garbarino,² Andrei Rogalev,² and Thierry Ouisse^{1,†}

¹Université Grenoble Alpes, CNRS, Grenoble INP, LMGP, F-38000 Grenoble, France

²European Synchrotron Radiation Facility (ESRF), CS 40220, F-38043 Grenoble Cedex 9, France

³Graduate School of Engineering, Nagoya University, Nagoya 464-8603, Japan

⁴Nagoya University Synchrotron Radiation Research Center (NUSR), Nagoya University, Nagoya 464-8603, Japan

⁵Université Grenoble-Alpes, CEA, IRIG, PHELIQS, F-38054 Grenoble, France

⁶Université Grenoble-Alpes, Grenoble INP, CNRS, F-38042 Grenoble, France

⁷Department of Materials Science and Engineering, Drexel University, Philadelphia, Pennsylvania 19104, USA

⁸Synchrotron-SOLEIL, L'Orme des Merisiers, Saint-Aubin 91192, France

 (Received 19 July 2020; revised 22 September 2020; accepted 22 September 2020; published 16 October 2020)

Herein we show that Mo₄Ce₄Al₇C₃, a recently discovered nanolamellar compound displaying mixed valence, combines Kondo lattice behavior with ferromagnetism. A sizeable magnetization is carried by 3*p* states of Al as evidenced by a strong x-ray magnetic circular dichroism signal at the *K* edge of aluminum, whereas no detectable signal was observed at the *K* edge of carbon and *L*_{2,3} edges of molybdenum. These results point out that the ferromagnetic behavior originates in the Ce atoms with 4*f*¹ electronic configuration lying within the Al planes. The evolution with pressure of the mixed valence of Ce atoms in the Mo-C planes determined via Ce *L*₃ x-ray-absorption spectra along with the magnetoresistance measurements across the ferromagnetic transition unambiguously reveal a Kondo behavior. Angle-resolved photoemission spectroscopy and density functional theory confirm a certain degree of Ce 4*f* electron delocalization. More generally, conduction electrons are not restricted to lie in the MoC planes but are also delocalized in the Al planes.

DOI: [10.1103/PhysRevB.102.155121](https://doi.org/10.1103/PhysRevB.102.155121)

I. INTRODUCTION

Cerium-based intermetallic compounds are known for the wealth of interesting physical effects they display. The Ce location at the beginning of the lanthanide series is often responsible for inducing a mixed valence of the Ce atoms [1–3]. This mixed valence, the localized character of the Ce 4*f* orbitals, and the coupling between the Ce degenerate electron states and the delocalized conduction-band electrons are key ingredients at the heart of most of the noteworthy phenomena taking place in such compounds [2,3]. They sometimes form heavy fermion systems [2,4] that can lead to superconducting phases or a quantum critical regime [5]. Like other rare-earth-containing intermetallics, they are the materials of choice for studying Kondo impurity [3,6] and Kondo lattice [3,7] systems. Their magnetism can prove surprisingly complex (see, e.g., [8] or [9] for a recent experimental example). They have thus been one of the favorite hunting grounds for experimentalists and theoreticians interested in Kondo physics (see, e.g., [3] for a recent review).

At intermediate temperatures ($T > T_K$, the Kondo temperature), Ce-based intermetallics with Kondo behavior exhibit electron transport properties characteristic of the Kondo

impurity model [10]. However, at lower temperatures, coherence between the Ce sites sets in, so that the compounds behave as Kondo lattices [11,12]. Resistivity ultimately decreases as T tends towards zero [1], instead of exhibiting the usual logarithmic increase and saturation predicted by the impurity model [10,13]. While Kondo interactions result in spin-flip scattering processes above T_K [10], below it (at least in the impurity regime), antiferromagnetic (AFM) coupling between the occupied Ce sites and the surrounding conduction electrons leads to a singlet Kondo state [1]. It is therefore rather unusual to find simultaneously Kondo and ferromagnetic (FM) signatures. Yet, in recent years, such behavior has been reported for phases as diverse as Ce₄Rh₄Ge₃ [14], CePd₂P₂ [15], CeTiGe₃ [9,16–18], and CeRuPO [19]. Actinide based heavy fermion compounds such as UBe₁₃ [20] and Np₂PtGa₃ [21] also display both Kondo and FM characteristics. To focus but on one particular example, Ce₄Rh₄Ge₃ exhibits mixed valence, has two inequivalent Ce lattice sites, and combines a particularly clear FM transition with the magnetotransport properties associated with a Kondo lattice [14].

Herein we investigate Mo₄Ce₄Al₇C₃, a triclinic crystal system with a nanolamellar structure [22] that combines FM and Kondo system properties. This compound, recently discovered in Linköping in Sweden, was found to be FM below $T_C = 10.5$ K [22]. A very attractive feature of this compound is that single crystals (SCs) can be mechanically exfoliated, which would allow for the investigation of magnetism as a

*Corresponding author: maxime.barbier@grenoble-inp.fr

†Corresponding author: thierry.ouisse@grenoble-inp.fr

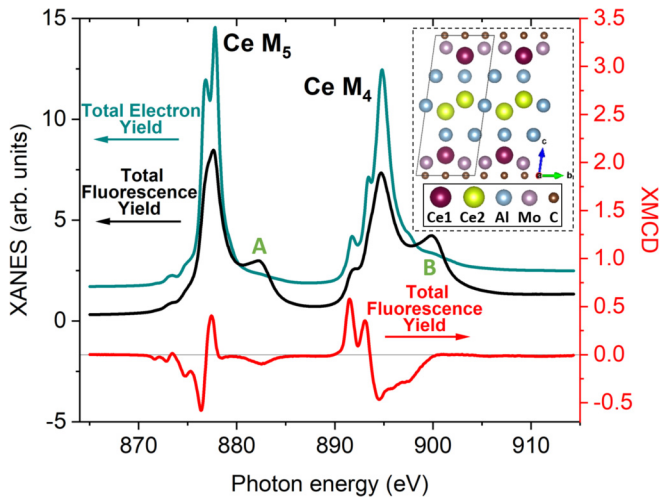


FIG. 1. Normalized XANES spectra measured with the total fluorescence yield (TFY) and total electron yield (TEY) (left axis) along with the TFY XMCD spectrum (right axis, same scale as XANES) at the Ce $M_{4,5}$ edges, at $T = 4.2$ K and $H = 1$ T. Features of interest are labeled with capital letters and identified in the text. The upper inset shows the crystal structure of $\text{Mo}_4\text{Ce}_4\text{Al}_7\text{C}_3$ as seen from the a axis, where the two inequivalent Ce sites are identified. A comprehensive depiction of that structure can be found in [22].

function of thickness, down to a thickness of half a unit cell [23]. Although this phase does not strictly obey the stoichiometry rules usually attached to the definition of a MAX phase [24,25], its crystal structure makes it a close cousin of this well-known family of nanolamellar carbides and nitrides (MAX phase formula is $M_{n+1}AX_n$, with M a transition metal, A belongs mainly to groups 13–14, $X = \text{C}$ or N and $n = 1–3$). Like the MAX phases, the structure is an ordered stack of two-dimensional (2D) carbide planes separated by A atom layers (here A is Al) [22]. The carbide layers incorporate Mo, C, and Ce atoms exactly as in the i -MAX family discovered quite recently [26,27]. There are two inequivalent Ce lattice sites (see inset of Fig. 1) [22] in this structure. Thereafter, the Ce sites belonging to the carbide layers will be labeled Ce1. However, and in contrast with their i -MAX counterparts, the Al layers separating the carbide layers are not single layers, but triple layers including an ordered honeycomb sublattice of Ce atoms (labeled Ce2) embedded in the middle of Al layers (see inset in Fig. 1) [22]. The main orbital contribution to the conduction band is that of the d orbitals of the Mo atoms [22]. The Ce2-Ce2 intersite distance in the Al planes is substantially shorter than the Ce1-Ce1 intersite distance in the Mo-C planes. The two Ce sites are thus markedly different. Moreover, the Ce atoms show a mixed valence behavior as we recently demonstrated using x-ray absorption near edge structure (XANES) spectroscopy [22].

Following the discovery of this compound, we showed that neither the Mo atoms nor the Ce atoms in $4f^0$ configuration exhibit any detectable x-ray magnetic circular dichroism (XMCD) below the FM transition [22]. This fact favors the hypothesis that (i) only the Ce2 sites are involved in the FM and (ii) the mixed valence is restricted to the Ce1 sites. In this work, we investigate further the respective contributions of the

two different Ce sites to the electronic and magnetic properties, and put forward complementary experimental evidence of the suggested model, as obtained by a thorough XMCD study of all chemical elements constituting the compound.

In rare-earth compounds, the magnetic state is often the result of a competition between magnetic order through Ruderman-Kittel-Kasuya-Yosida (RKKY) interactions and magnetic screening by the conduction electrons through Kondo interactions. Herein we combine various techniques to evidence and analyze the Kondo and FM properties of the $\text{Mo}_4\text{Ce}_4\text{Al}_7\text{C}_3$ crystal, and shed light on the role played by the two nonequivalent Ce sites. First, x-ray absorption, measured at the edges of Ce, Al, and C atoms allowed us to assign the FM to one of the two cerium lattice sites (Ce2), while the other is found to be in a mixed valence state (Ce1). The pressure-dependent evolution of this mixed valence hints at a rise in the conduction electron density with p . Magnetoresistance scaling and specific heat reveal the Kondo impurity regime and its competition with ferromagnetism. Increasing p is found to favor the Kondo regime at the expense of the FM state, which can be explained by the aforementioned rise in the density of conduction electrons and the variation of the exchange coupling constant. This Kondo/FM competition implies that the conduction electrons are not confined to the carbide planes containing the mixed valence Ce sites, but are also delocalized in the planes of the FM Ce sites. Angle-resolved photoemission spectroscopy (ARPES) measurements combined with density functional theory (DFT) brings additional credibility to this result.

II. EXPERIMENTAL METHODS

Single-crystal growth. We used a flux growth technique at high temperature, with typical, initial elemental ratios $x_{\text{Mo}} = 0.1$, $x_{\text{Ce}} = 0.4$, and $x_{\text{Al}} = 0.5$ before carbon incorporation. The growth reactor is induction heated. The elements are mixed and heated, in a sealed graphite crucible, to a maximum T of 1800°C for 1 or 2 h. The growth reactor is then slowly cooled down to 1000°C in 4–7 days. The source of C is the graphite crucible walls at high T . Depending on the temperature cycle and initial Ce content, typical C concentrations in the flux may range from $x_{\text{C}} = 0.2–0.4$, as estimated from crucible weighting before and after growth. The crucible is sealed in order to limit evaporation. Upon cooling to room temperature (RT), single crystals (SCs), are extracted from the flux by oxidizing the latter for a few days inside a chamber equipped with an air flux bubbling in water. The crystal-growth process is described in more detail in previous references [22,28,29]. The $\text{Mo}_4\text{Ce}_4\text{Al}_7\text{C}_3$ SCs are thin flakes, that grow preferentially along their basal planes. Maximum SC areas are a few mm^2 and their thickness ranges from 10 to $100\ \mu\text{m}$.

XANES and XMCD. The XANES and XMCD spectra at the $M_{4,5}$ edges of Ce and the K edge of Al and C were measured at the DEIMOS beamline at the French synchrotron radiation facility SOLEIL. The end station is equipped with a cryomagnet providing a 7 T magnetic field H , parallel to the x-ray beam, and sample temperatures down to 4.2 K. The absorption spectra were recorded simultaneously in two ways using (i) total electron yield (TEY) and (ii) total fluorescence

yield (TFY). The uncapped Si photodiode is located inside the magnet at 60° with respect to the beam. The x-ray beam reached the sample with an angle of 10° from the normal to the sample surface (close to the magnetic easy axis), so as to enhance the solid angle of the Si photodiode located aside in the split-pair magnet. Measurements have been performed on uncleaved, as-grown crystals. The beam line, equipment, resolution, and methods are thoroughly described in Refs. [30] and [31]. The XMCD signals were obtained by reversing the helicity of x rays with fixed direction of the magnetic field. In order to eliminate experimental artefacts, the XMCD signals were also recorded for reversed direction of the magnetic field. The TFY spectra at the Al and C *K* edges were corrected for self-absorption effects.

The high-pressure XANES spectra were measured at the European Synchrotron Radiation Facility (ESRF) ID12 beamline [32] using the partial fluorescence yield (PFY) detection mode with a silicon drift diode detector mounted in a backscattered geometry. An as-grown single-crystal flake of dimensions $\sim 100 \times 100 \times 20 \mu\text{m}^3$ was placed into a diamond-anvil cell (equipped with a partially perforated front anvil with a 600 μm diameter culet size) loaded with He gas to ensure good hydrostatic conditions. The measurements were carried out at 300 K up to a pressure of 19 GPa. The pressure was measured *in situ* using ruby luminescence. The experimental spectra were corrected for self-absorption effects. The XANES spectra are analyzed assuming that they are a sum of two contributions due to the $4f^0$ and $4f^1$ electronic configurations of the Ce atoms. Each of the two peaks is approximated by a “white line” ($2p \rightarrow 5d$) fitted with a Gaussian function and transitions into a continuum represented by an arctangent function. The $4f$ valence of Ce atoms is then estimated as the ratio of the areas of the respective Gaussians (A_1 for $4f^1$ and A_0 for $4f^0$), given by $V = A_1/(A_1 + A_0)$. More details regarding the fitting procedure can be found in Ref. [22].

Magnetotransport. Magnetotransport was investigated by measuring the resistivity ρ as a function of H and pressure in a modified Bridgman cell with ceramic anvils, as described in [33]. The pressure-transmitting medium was Fluorinert. The current was applied in the *a-b* plane and H up to 9 T was applied in the out-of-plane direction. The p was determined at low temperature from the superconducting transition temperature of a piece of lead positioned in the cell next to the sample.

Specific heat (c_p). The constant pressure heat capacity measurements were carried out at Institut Néel in Grenoble, using a commercial Quantum Design PPMS, in the 0.4–300-K temperature range. The measurements are based on the relaxation method, and the raw data were systematically corrected from the contributions of the platform and the Apiezon N grease used to glue the crystal on the platform. The sample was a flakelike single crystal weighing 0.54 mg and was lying flat on the c_p platform, with the applied magnetic field in the out-of-plane direction, which is close to the magnetic easy axis.

ARPES. Measurements were carried out at the Cassiopée beamline of SOLEIL. Crystals were cleaved *in situ* under UHV conditions and measured using photon excitation energies out of or at the resonant $4d - 4f$ mode. Excitation

energies were varied from $h\nu = 100$ to 137 eV, with an energy resolution ΔE below 10 meV, with $p < 3 \times 10^{-9}$ Pa and $T = 14$ K. ARPES was measured in the *S*-polarization mode configuration. A precise description of this mode as well as angle definitions and configurations can be found in Fig. 1 of Ref. [34].

Density functional theory (DFT). All calculations were performed with the full potential LAPW + lo method implemented within the WIEN2K software [35]. The standard spinless Perdew-Burke-Ernzerhof (PBE) generalized gradient approximation (GGA) functional was chosen [36]. Both standard DFT as well as DFT + U calculations were performed, and an orbital dependent Hubbard potential U of 7.074 eV was applied to the $4f$ orbitals of the Ce atoms. $U \approx 7$ eV roughly bounds the interval of reasonable values for Ce atoms. Wave functions were expanded up to a *RKM* cutoff parameter of 9 to guarantee that convergence was reached (*RKM* refers to the product of the smallest “atomic sphere radius” R times the largest K vector of the LAPW expansion used). A $16 \times 16 \times 6$ Monkhorst-Pack cell was used. For band-structure plots, denser k meshes of 1200 k points were chosen. The overall level of convergence in energy was set to 0.01 mRy. Here it is important to stress that for mixed valence Ce compounds, use of a DFT + U method is not always sufficient, and for a more involved analysis, more complex computational methods such as DFT + DMFT are clearly required. Our DFT and DFT + U results can therefore not catch all quantitative aspects of the electronic structure in a fully satisfying fashion. However, the agreement often obtained between ARPES and DFT for bands not involving substantial Ce contributions obviously strengthens the plausibility of the analysis conducted here using all other experimental data.

III. RESULTS AND DISCUSSION

A. XANES and XMCD

Figure 1 compares the XANES recorded with TFY and TEY at the Ce $M_{4,5}$ absorption edges under a magnetic field of 1 T. The fine structures visible at the Ce $M_{4,5}$ edges arise from the multiplet structure of the final states of the $4f^1$ and $4f^0$ ground states’ electronic configurations of both the Ce1 and Ce2 sites. Different spectral features can be observed in the XANES spectra, i.e., contributions from $\text{Ce}^{3+}(f^1)$, $\text{Ce}^{4+}(f^1L)$, and $\text{Ce}^{4+}(f^0)$ states [37,38], the latter often referred to as the “ f^0 satellite” appearing at the higher energy side (~ 5 eV, features *A* and *B* in Fig. 1) of the leading XANES peak.

From our TEY measurements, the amount of $4f^0$ reflected by the contribution of the “ f^0 satellite” in the XANES spectrum is as small as in the Ce $M_{4,5}$ spectra recorded in CeCu_2Si_2 and CeRu_2Si_2 , where Ce is almost trivalent [39,40]. Surprisingly, the Ce $M_{4,5}$ TEY spectrum of $\text{Mo}_4\text{Ce}_4\text{Al}_7\text{C}_3$ is characteristic of a monovalent $4f^1$ Ce compound and does not show any feature typical of a $4f^0$ contribution that could be expected from oxidized Ce atoms at the surface of the sample [41]. A plausible interpretation of this observation is that the outermost Al and/or Mo-C layers could form native oxide layers (e.g., Al_2O_3) that prevent transformation of Ce $4f^1$ atoms into $4f^0$. It is not excluded that this barrier layer could lead

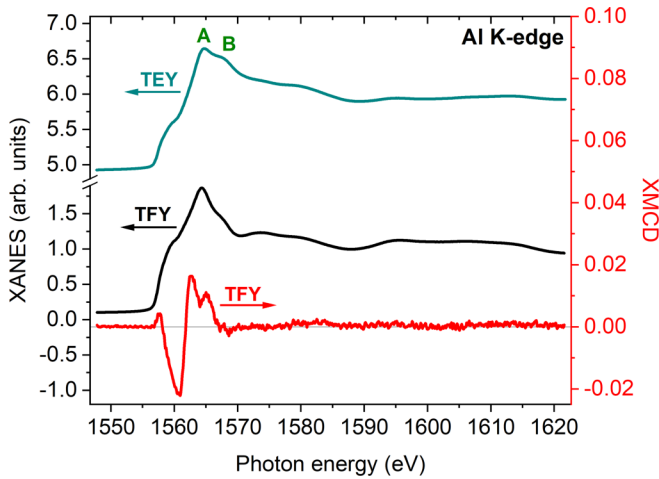


FIG. 2. Normalized TFY and TEY XANES spectra (left axis) along with the TFY XMCD spectrum (right axis, same scale as XANES) at the Al K edge, for $T = 4.2$ K and $H = 1$ T. The TFY XANES were corrected for self-absorption effects. Features of interest are labeled with capital letters and discussed in the text.

to an extensive redistribution of the electronic densities near the surface of the crystal. The existence of this oxide barrier is supported by the TEY detected XANES spectra of aluminum. The Al K -edge XANES spectrum (Fig. 2) exhibits two broad features at 1565 and 1568 eV, labeled A and B, respectively. The latter is characteristic of Al_2O_3 [42,43] whereas the former feature arises from Al atoms in the $\text{Mo}_4\text{Ce}_4\text{Al}_7\text{C}_3$ phase. Indeed, the B feature is found much weaker in the Al K -edge spectrum measured with TFY, which is more bulk sensitive.

In contradistinction to the TEY spectrum, the more bulk sensitive TFY measurements show a strong contribution of the $4f^0$ state (Fig. 1). It must be noted that the TFY spectra, recorded in the soft x-ray range at M edges of rare earths and/or L edges of $3d$ transition metals, are generally quite different from actual x-ray absorption, due to the final-state effects and inelastic decay processes [44,45]. In the case of Ce at the $M_{4,5}$ edges, the multiplet peaks are usually smeared out in comparison to the true absorption spectra and the lower energy structures appear less intense with respect to those at higher energy [46]. Therefore, these data can be interpreted only qualitatively. However, the presence of $4f^0$ configuration is evident in the $M_{4,5}$ TFY spectra and this is consistent with the mixed valence state of Ce determined previously from the Ce L_3 edge [22].

Unfortunately, the XMCD spectrum recorded with TFY at the Ce $M_{4,5}$ absorption edges is distorted by reabsorption effects and application of the sum rules to deduce spin and orbital magnetic moments carried by the $4f$ electrons of Ce is therefore not possible. However, the intensity of the XMCD signal is proportional to the total $4f$ magnetic moment and we can monitor it as a function of applied field in order to obtain the Ce magnetization curves. The curves recorded at the first maximum of the Ce M_4 XMCD signal (at 891.5 eV) below (4.2 K) and above (18 K) the Curie temperature, with H applied close to the c^* axis of the crystal, are shown in the inset of Fig. 3. A paramagnetic behavior expected for Ce ions in the $4f^1$ configuration is observed in the

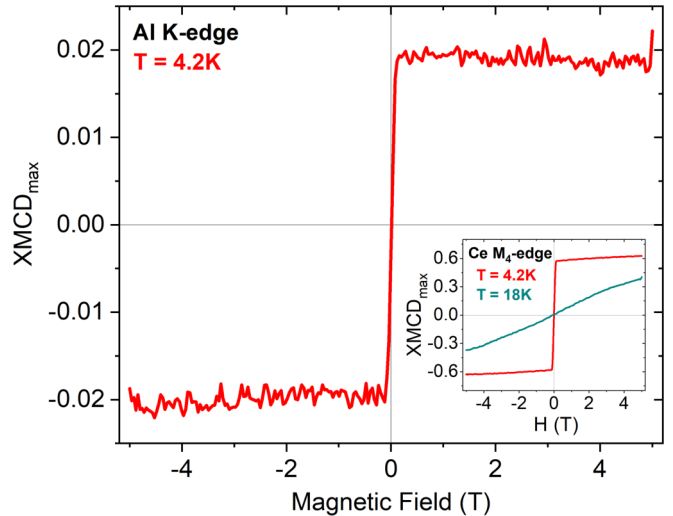


FIG. 3. Element-specific TFY XMCD intensity vs H measured at the Al K edge at $E = 1560.5$ eV for $T = 4.2$ K and at the Ce M_4 edge at $E = 891.5$ eV for $T = 4.2$ K and $T = 18$ K (inset). Intensities are normalized to match those of the TFY XMCD spectrum at these energies.

high-temperature curve. The low-temperature magnetization curve is very similar to the macroscopic magnetization [22], which confirms that TFY-XMCD is a measure of bulk properties. In addition to the FM jump, the XMCD magnetization exhibits a paramagnetic-like evolution as H is increased, as observed macroscopically. This behavior may indicate that there are two magnetic states of Ce in $\text{Mo}_4\text{Ce}_4\text{Al}_7\text{C}_3$ below the Curie temperature, i.e., ferromagnetically ordered and paramagnetic. This interpretation was already inferred from the absence of XMCD signal from Ce atoms in the $4f^0$ configuration (i.e., no XMCD signal at the energy of the $4f^0$ peak) in the $L_{2,3}$ -edges spectra [22], suggesting that the mixed valence Ce1 site is not involved in ferromagnetic interactions. Moreover, no sizeable XMCD was observed on the Mo atoms under a modest magnetic field of 1 T, as opposed to what could be expected if the Ce1 site was FM, because of the proximity of Ce1 and Mo in the Ce/Mo planes [22]. In order to confirm that the Ce2 site is the only one involved in FM interactions, one must therefore also examine the magnetic properties of aluminum and carbon atoms using XMCD.

The XANES and XMCD spectra recorded at the Al K edge are shown in Fig. 2. The XANES spectral shape reflects the Al empty density of states of p symmetry and from this perspective resembles the K -edge spectra measured for metalloids, e.g., Ge or Si [47,48] in intermetallics. A strong XMCD signal, as high as 1.5% with respect to the edge jump, is observed at the Al K edge. This signal provides evidence that the Al $3p$ states are magnetically polarized in the FM state of $\text{Mo}_4\text{Ce}_4\text{Al}_7\text{C}_3$. The integrated intensity of the XMCD signal is proportional to the magnitude of the orbital magnetic moment induced in the $3p$ band. This orbital magnetic moment is induced by a large spin-orbit interaction [49–52], in the present case between $3p$ (Al) and $4f5d$ (Ce). A similar mechanism is, for instance, responsible for the orbital polarization of Ge in UGe_2 [53]. The field dependence of the Al K -edge XMCD

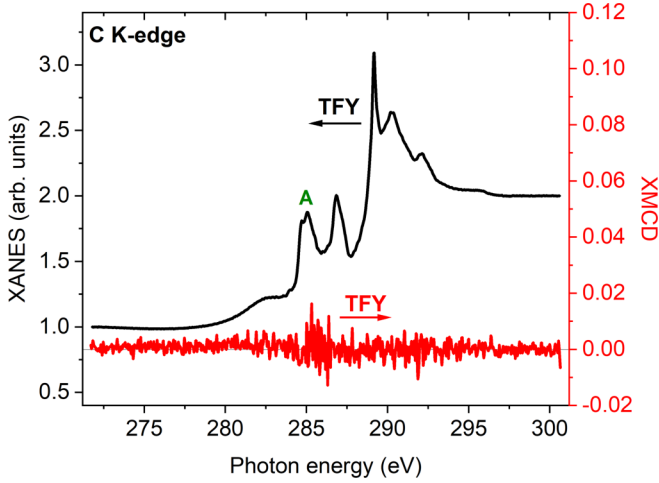


FIG. 4. Normalized TFY and TEY XANES spectra (left axis) along with the TFY XMCD spectrum (right axis, same scale as XANES) at the C K edge, for $T = 4.2$ K and $H = 1$ T. The TFY XANES has been corrected for self-absorption effects. Features of interest are labeled with capital letters and identified in the text.

signal measured at 1560.5 eV is plotted in Fig. 3. This curve is similar to the one recorded at the M_4 edge of Ce, so that one can conclude that the Al $3p$ states are involved in the FM coupling between Ce2 sites. Such a contribution of Al to the magnetism of a compound was, for instance, previously found in UCoAl [54]. However, it is worth noting that the Al magnetization saturates above 0.2 T, and does not display the paramagnetic (PM) behavior observed at the Ce M_4 edge. This could suggest that the Ce PM contribution is due to Ce atoms in the $4f^1$ configuration occupying the Ce1 sites.

Figure 4 plots the XANES spectrum recorded at the C K edge in the TFY mode. It clearly shows sharp features similar to those reported in the literature [55,56]. Most important for the present study is the absence of a clear XMCD signal at the K edge of carbon within the noise level of our experiment. Previous reports on induced magnetism of C atoms, e.g., in Fe/C multilayers, graphene at Ni(111) or YIG interface and C₆₀ molecules at Fe(001), have all shown that a finite XMCD signal occurs at transitions of the $1s$ electron into the π^* states (XANES peak labeled A in Fig. 4) [57–60] which is significantly larger than the noise level in our data. The absence of a clear magnetization on the carbon atoms also suggests that only Ce2 sites are ferromagnetically coupled and the mixed-valent Ce1 sites remain paramagnetic below the Curie temperature.

B. Ce mixed valence

Variation of the Ce mixed valence with pressure has been studied with Ce L_3 edge XANES spectroscopy at room temperature. Figure 5(a) shows the XANES spectra recorded at $p = 0.76$ and 18.9 GPa. The energies of the $4f^0$ and $4f^1$ Ce configurations are separated by a strong core-hole potential, so that in a mixed valence state the XANES spectrum exhibits two peaks [22]. As shown in Fig. 5(b), the proportion of $4f^1$ states steadily decreases in favor of the $4f^0$'s with increased p : The ratio of $4f^1$ states, defined as $4f^1/(4f^0 + 4f^1)$, decreases

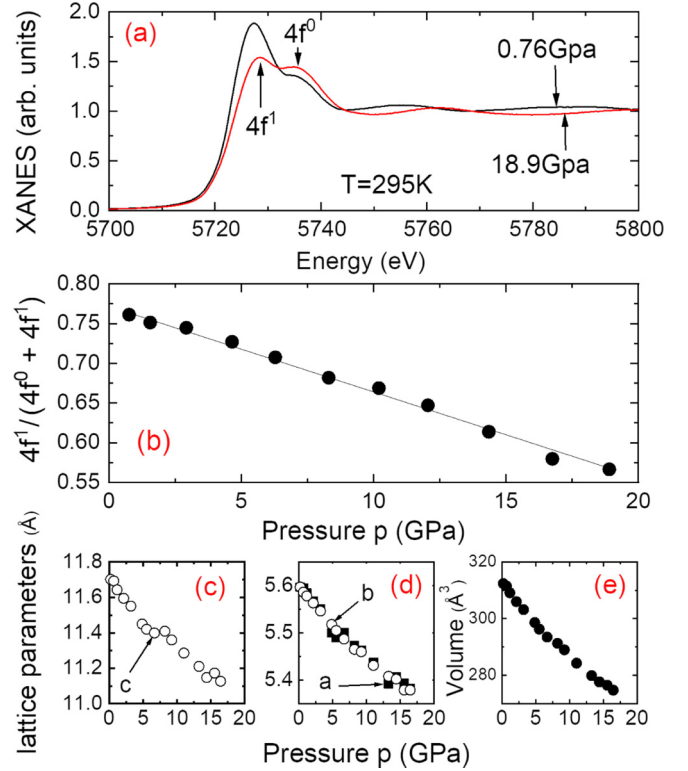


FIG. 5. Dependence of the Mo₄Ce₄Al₇C₃ mixed valence on applied pressure. (a) Normalized XANES spectra measured at the Ce L_3 edge for $p = 0.76$ GPa and $p = 18.9$ GPa, at $T = 295$ K. (b) Evolution of the valence with applied p . (c)–(d) Evolution of the lattice parameters with applied pressure. At 0.67 GPa $\Delta c/c = 4.8 \times 10^{-2}$ and $\Delta b/b = \Delta a/a = 3.8 \times 10^{-2}$. (e) Evolution of unit cell volume with p .

from around 0.75 at 0.76 GPa down to 0.55 at 18.9 GPa. This behavior is indeed expected for a system with strongly delocalized $4f$ states being hybridized with the surrounding atomic orbitals. Unfortunately, the maximum available pressure did not allow us to reach a possible saturation at 0.5, where all Ce1 sites are occupied by Ce ions in the $4f^0$ configuration while the FM Ce2 sites remain fully $4f^1$.

We also measured the dependence of the lattice parameters as a function of pressure at the ID27 beamline at the ESRF and did not observe any strong anomaly in the studied range. A smooth variation of lattice parameters and unit cell volume at 295 K seems to be in line with the linear dependence of the mixed valence [see Figs. 5(c)–5(e)]. The observed decrease of the mixed valence should lead to a sizeable increase in the electron density in the conduction band. This observation will be taken into account when discussing the effect of pressure on the magnetotransport properties expounded upon the next section.

C. Magnetotransport

Figure 6 plots the dependence of the resistivity, ρ , with temperature and applied p . At $p \approx 1$ bar, ρ displays a wide bump at intermediate temperatures (50–300 K), characteristic of mixed valence compounds [1]. At lower temperatures, a local minimum in ρ is observed for some pressures (e.g.,

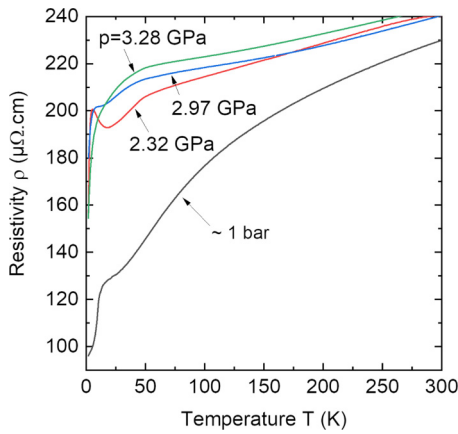


FIG. 6. Evolution of resistivity with temperature at various applied pressures.

2.32 GPa), below which ρ initially rises, characteristic of a Kondo impurity regime. On further cooling, ρ decreases as the Kondo impurity behavior is finally removed by the competing FM transition and/or the onset of the Kondo lattice regime [1]. At ambient p , the FM transition is revealed by a kink at T_C below which ρ abruptly drops. On increasing p , T_C decreases to about 3 K at 3 GPa, and extrapolates to $T = 0$ at about 4 GPa.

The competition between the Kondo impurity regime and the FM interactions is best shown by a quantitative analysis of the magnetoresistance (MR). Figure 7(a) plots the normalized MR in the 7–20-K range as a function of H normalized by H^* , which is the appropriate Kondo field at each T [determination of H^* is shown in Fig. 7(b)]. Although Fig. 7(a) only shows the results obtained at various T 's for $P = 2.32$ GPa, the MR at all other pressures tested falls on the same universal curve as in Fig. 7(a). At 2.32 GPa, MR scaling is suppressed roughly

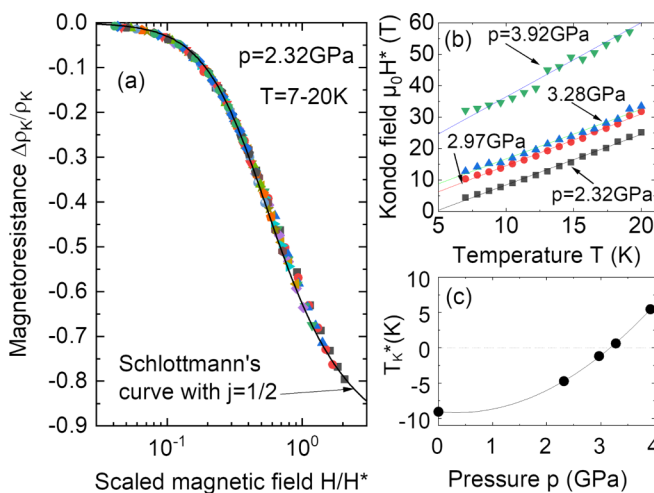


FIG. 7. Magnetoresistance measurements. (a) MR scaling in the Kondo regime for $P = 2.32$ GPa and T in the 7–20-K range, along with Schlottmann's theoretical MR for $j = 1/2$. (b) Kondo field vs temperature for various applied pressures (solid lines are linear fits to the data points). (c) Effective Kondo temperature vs applied pressure (solid line is a guide for the eyes).

below 6 K (not shown). Since the quality of the tested SCs is not very high [28,29], the low- T resistivity is ultimately limited by defect scattering [61]. We remove the contribution of this resistivity component, ρ_{imp} , from the Kondo contribution as follows. As can be seen for $p = 1$ bar (Fig. 6), a trend towards saturation is clearly seen below T_C , with ρ around $95 \mu\Omega \text{ cm}$ at 2 K. We thus expect ρ_{imp} to lie somewhat below this value. As the MR due to the Kondo effect reaches considerable values [85% drop in ρ at 9 T, Fig. 7(a)], we neglect the MR due to ρ_{imp} (in other MAX phase SCs, this MR component is around 0.5% at 9 T [61]). For $H = 0$, the overall resistivity variation in the range for which the MR scaling is observed is limited to a very few percent, and we also neglect it. A back-of-the-envelope calculation then shows that the Kondo MR $\Delta\rho_K/\rho_K^0$ is related to the measured MR $\Delta\rho/\rho^0$ by $\Delta\rho_K/\rho_K^0 \cong f \times \Delta\rho/\rho^0$ with $f = \rho^0/\rho_K^0 = (\rho_K^0 + \rho_{\text{imp}})/\rho_K^0$. Therefore we simply correct the as-measured values by a constant factor f . It is remarkable that by assuming $f = 1.75$, all scaled curves at all pressures fall on the quantitative MR model formulated some decades ago by Schlottmann [62] in the Kondo impurity regime and for the case with an effective $j = 1/2$ value [see Fig. 7(a)]. Assuming $f = 1.75$ gives ρ_{K0} around $71 \mu\Omega \text{ cm}$, and thus $\rho_{\text{imp}} \sim 54 \mu\Omega \text{ cm}$, in agreement with the resistivity value measured at 2 K. It was not possible to obtain acceptable fits using other values of j as input. The excellent agreement between the MR data and Schlottmann's model proves the existence of a Kondo impurity regime. The effective $j = 1/2$ value suggests that the Ce $4f^1$ state reduces to the lower Kramers doublet resulting from the crystal-field splitting induced by the triclinic structure, as already anticipated from our previous magnetization data [22]. In contrast to similar systems [20], we did not require to apply “unconventional” MR scaling.

In Fig. 7(b), extrapolating the plots of H^* versus T down to $H^* = 0$ results in an effective Kondo temperature T_K^* [63–65]. The extracted T_K^* 's are then plotted versus p in Fig. 7(c). Some of them are negative. This is not physically consistent with a system entirely ruled just by Kondo physics, and implies that T_K^* is not directly equal to the Kondo temperature T_K , but also reflects the existence of additional interactions [14,20,66]. Assuming that the magnetic moment gJH^* is more or less equal to the competing actions of thermal fluctuations, Kondo and FM interactions $gJ\mu_0 H^* \approx k_B T + k_B T_K - k_B T_C$ explains both the temperature dependence and the negative T_K^* values. This is further ascertained by the dependence of T_K^* on p [Fig. 7(c)]: T_K^* turns positive only for the largest accessible p 's [Fig. 7(c)]. As noticeable from both Figs. 6 and 7, increasing p clearly favors the Kondo regime and reduces T_C . This can be explained by the concomitant increase of mixed valence and conduction electron density already established from our XANES measurements. Increasing p results in (i) an increase in the number n of conduction electrons per Ce site and (ii) an increase in the exchange coupling constant J . J is the same for the RKKY and Kondo interactions, but T_K varies as $\exp(-1/nJ)$ whereas $T_{\text{RKKY}} \sim J^2$ [67]. These variations rule the phase diagram established using J and n as parameters [68]. The increase of J with p , combined with the increase of n , moves the system from the FM domain to the Kondo domain [7,8]. Since the Kondo regime competes with the FM interactions, this implies that the FM Ce2 sites are involved

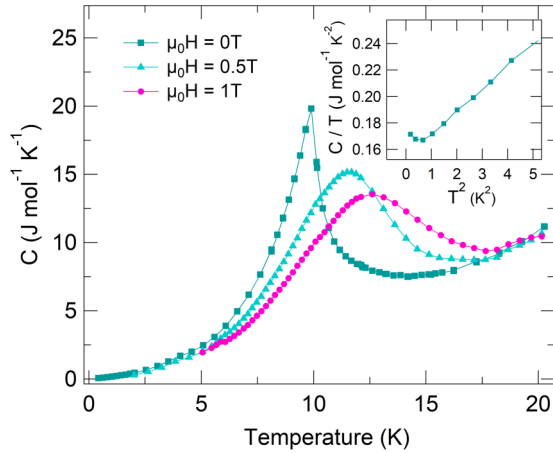


FIG. 8. Thermal variation of the specific heat of Mo₄Ce₄Al₇C₃ under magnetic fields up to 1 T. Inset shows low-temperature specific heat C/T vs T squared, at zero field.

in the Kondo regime, and thus that the conduction electrons are not restricted to lie mainly in the MoC planes, as was observed in the MC planes of some MAX phases [34,69], but are also delocalized in the Al planes. This point is confirmed in Sec. III E. Unfortunately, our data do not allow us to assert if the Ce1 atoms in the $4f^1$ state participate or not in the Kondo effect.

D. Specific heat

The temperature dependence of c_p is plotted in Fig. 8, for three values of H . At zero field there is a clear lambda anomaly with a maximum at 10 K. With increasing H , the anomaly gradually broadens and the maximum shifts to higher T . That behavior is consistent with our previous study [22] and confirms that the transition corresponds to FM ordering at $T_C = 10$ K. Within the molecular field approximation, the c_p jump at the magnetic transition for a FM system with effective moment $j = 1/2$ (as expected from the crystal symmetry and confirmed from the MR scaling above) is expected to be $\Delta c_{\text{mag}} = 12.46 \text{ J}/(\text{mol K})$ per ion participating to the FM. In our case, provided that the FM is carried by the Ce atoms sitting on the Ce2 sites (as mentioned above and in Ref. [22]), that jump is about $\Delta c_{\text{mag}} \approx 10 \text{ J}/(\text{mol K})$. This value is an overestimation, as it includes the background electrons and phonon contributions. It is therefore safe to assume that this jump is diminished with respect to the expected value, which is generally attributed to Kondo screening of the $4f$ electrons [70]. This further confirms the Kondo behavior of this compound.

The inset of Fig. 8 plots c_p/T vs T^2 down to $T = 0.4$ K. The FM transition at $T_C = 10$ K being very wide, its influence is still significant at such temperatures, keeping us from inferring the Sommerfeld coefficient γ_0 from this plot. That is usually done by extending the straight portion of this plot down to $T = 0$ K, which then intersects the c_p/T axis at γ_0 , where γ_0 corresponds to the electronic contribution to c_p . However, since c_p can only be overestimated in those circumstances, we can safely say that γ_0 is below the lowest value of c_p/T , that is $\gamma_0 < 167 \text{ mJ}/(\text{mol K}^2)$. It can also be expected

that γ_0 is still sizeably enhanced with respect to non-Kondo systems, because of the correlation effects among $4f$ electrons [19]. It is also worth noting that the lowest temperature points display an upturn of c_p/T . That phenomenon is commonly observed in such compounds, and is likely caused by a Zeeman splitting on nuclei with nonzero spin [21,71]. It must be stated that attempts to grow single crystals of an isostructural La-based compound were unsuccessful, and therefore such crystals could not be used as a reference to isolate the Ce $4f$ contribution to c_p . For the time being, this is keeping us from performing a deeper analysis of our data.

E. ARPES

The ARPES spectra were measured at $T = 14$ K, which is in the paramagnetic state, slightly above the FM transition. Figure 9 compares ARPES and DFT + U near the Fermi-level band structure along the in-plane axis ΓM (in Fig. 9 k_{\parallel} variation of the ARPES maps is obtained by varying the angle at a constant photon energy; see, e.g., Refs. [34,69,72,73]). Figures 9(c) and 9(d) show the ARPES dispersion signal versus detector energy, both in the $4d$ - $4f$ on resonant and nonresonant modes, and Fig. 9(b) shows a spectrum integrated over the angular range in the $4d$ - $4f$ resonant mode. In Fig. 9(b), one can clearly observe the Ce $4f^0$, $4f^1_{7/2}$, and $4f^1_{5/2}$ (Kondo resonance) final states, as for other Ce-based Kondo systems (see, e.g., [74]). The hybridization of the near-Fermi-level states with the Ce $4f^1$ state is also clearly visible in the resonant mode (and discussed further below). Although the $4f^0$ final state is very intense [Fig. 9(b)], suggesting a prevailing $4f^1$ initial state, it can however not be used as a quantitative probe of the mixed valence for, even if the crystals were cleaved in UHV conditions, it is well known that the contribution of Ce's at the cleaved surface can dramatically affect the intensity ratio between the various peaks [75] (in our case, we know that cleavage takes place at the less strongly bonded Al planes, so that the surface necessarily includes Ce atoms [23]). It is worth noting that from Fig. 9(b), the initial $4f^1$ state ($4f^0$ final state) is almost nondispersive. However, and as explained in detail below, combining the dispersions observed and predicted in Figs. 9(c) and 9(d), as well as in Fig. 10, lends strong support to the fact that the dispersion curves we evidence are those of bulk states.

As explained in Sec. II, our DFT and DFT + U approaches does not allow us to give a fully reliable account of the Ce contribution to the electronic structure. However, it has already been noted that such an approach can still give a meaningful, qualitative account of the bands not involving Ce or involving Ce-dispersive states [76]. In the previous sections we deduced from the XMCD, XANES, and MR data that delocalized electrons had to interact with the Ce2 sites, which are located in the Al planes. In most MAX phases, there is always some in-plane delocalization in the carbide planes, but here, our data also imply to combine this Mo-C, in-plane delocalization with an additional delocalization of the conduction electrons along k_z . Therefore, some E versus k_z dispersion curves must cross E_F . This can be further confirmed by combining DFT and ARPES data, as explained below.

As expected, a reasonable similarity is obtained for bands lying from 0.2 to 1.2 eV below E_F , which mainly involve Mo

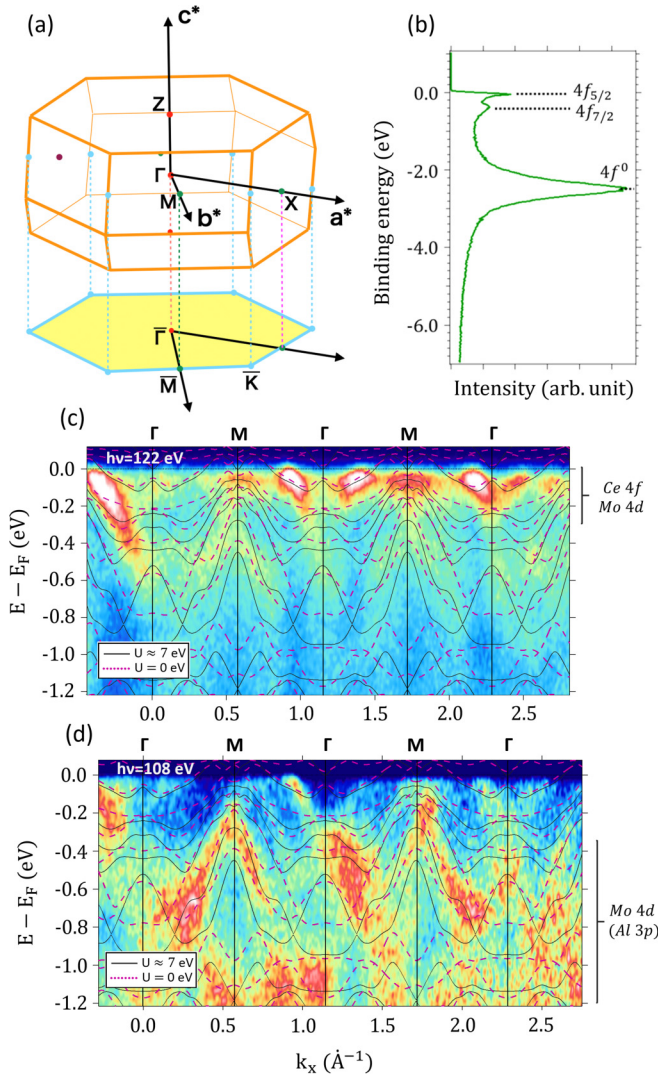


FIG. 9. (a) Relation between the triclinic Brillouin zone (BZ) (orange lines) of $\text{Mo}_4\text{Ce}_4\text{Al}_7\text{C}_3$ and a k_z (c^*) projected hexagonal BZ (light blue lines). (b) Integrated spectra of a $\text{Mo}_4\text{Ce}_4\text{Al}_7\text{C}_3$ single crystal over a specific direction, with $h\nu = 122$ eV. The intense flat band at 2.2 eV below E_F corresponds to the $4f^0$ final states, while clear dispersive features close to E_F are visible and coexist with the peak corresponding to the $4f_{5/2}^1$ together with nondispersive $4f_{7/2}^1$ final states. On-resonance (c) and off-resonance (d) ARPES mapping over approximate out-of-plane coordinate (due to a strong k_z broadening) compared with band structures over ΓM extracted from DFT or DFT + U calculations, with $U = 7.074$ eV. Bands that show a stronger Ce character dominate the on resonance spectra while Mo bands appear more clearly on the off resonance spectra.

orbital contributions. The ARPES signal intensity of those bands is not enhanced in the on resonant $4d$ - $4f$ excitation mode ($h\nu = 122$ eV), due to their weaker $4f$ orbital character [Fig. 9(b)]. In contrast, the strong enhancement of the ARPES signal at all bands crossing points with E_F in the resonant mode [compare Figs. 9(c) and 9(d)] is a clear manifestation of the strong coupling between the Ce degenerate electron states and the delocalized conduction-band electrons, as expected for a Kondo system.

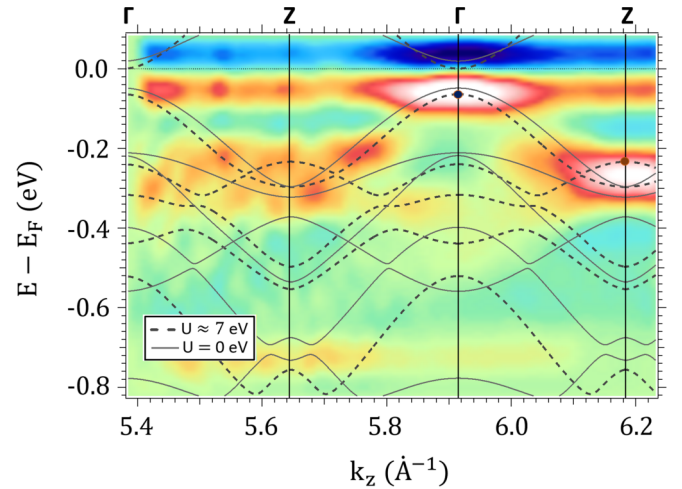


FIG. 10. Out-of-plane ARPES mapping over ΓZ , obtained by varying $h\nu$ from 100 to 137 eV, and compared with DFT and DFT + U bands. The two dots refer to specific points of band 90 (located in Γ and Z , respectively) which are used in the text and also shown in Fig. 11. This band does not only exhibit a strong k_z dispersion, as demonstrated in this figure, but also crosses the Fermi level, as shown in Fig. 11.

Figure 10 compares the DFT and ARPES dispersions along ΓZ (in Fig. 10, k_z variation is obtained by plotting the ARPES intensity at incident photon energies varying from 100 to 137 eV, using an inner potential of 15.12 eV; see, e.g., Ref. [34]). Figure 10 evidences strongly dispersive bands along k_z . Furthermore, the ARPES results seem to be in reasonable agreement with the DFT in many regions. Although from the ARPES data it is not clear whether, along this precise crystallographic axis, those bands really cross E_F or just touch it, what is clear is the Al-Ce planes contribute to the electronic structure close to E_F , and that DFT gives a reasonable account of the observed variations. Besides, the ARPES signal broadening, appearing in most dispersions in Fig. 9, is clearly related to k_z broadening, and not energy resolution. This broadening is in turn related to the k_z dispersion of the energy bands, indicating again that we do probe bulk properties (simple lifetime effects would not result in such a broadening).

This suggests that even if our calculation method does not take into account the dynamical effects required for a quantitatively accurate evaluation of the bands close to E_F , and even if we should obviously not rely entirely on such an approach, we can use DFT + U as an additional, reasonable indicator, and examine the dispersion along some particular directions, even if such directions would be difficult to observe experimentally. Figure 11 is such an example: dispersions were plotted along ΓX and ZX' [lines are defined in Fig. 11(b)]. In Fig. 11(a), each particular band is therefore represented by two different curves (solid and dotted lines). From Fig. 11(a), one observes that some bands do not cross E_F at the same in-plane k_x coordinate, depending on whether one spans the ΓX or the ZX' direction. This is the signature of a k_z dispersion of that band.

To better understand that point, focus on the particular band for which, in Fig. 11(a), we connected the two corresponding

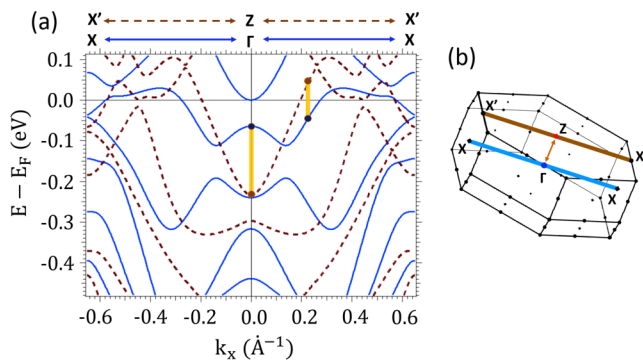


FIG. 11. (a) DFT + U band structure over ΓX and ZX' , with the directions and the triclinic BZ of Mo₄Ce₄Al₇C₃ given in (b). The effect of k_z broadening on band 90 is highlighted by the yellow lines, thus indicating a significant k_z delocalization of the conduction band.

curves by two vertical, yellow line segments at two different values of k_x . For a given k_x value, the length of the yellow line segment is equal to the energy difference between the two chosen planes in the same band. For instance, for $k_x = 0$, the line segment goes from Γ to Z and gives us back the full width of the band dispersion along k_z , as directly observed in Fig. 10 for the same band (see the energy difference between the blue and red points reported in Fig. 10). The second line segment, which crosses E_F , clearly shows that for that particular k_x value, the corresponding band is dispersive through E_F , and implies that some electrons are truly delocalized along k_z . Plotting the Fermi surface (not shown) also indicates that the surface normal exhibits a non-negligible k_z component in some particular regions. Those considerations support our previous conclusions: conduction electrons are not confined to Mo-C planes, but are also delocalized in the Al planes. The latter explains why the FM Ce2 atoms are also subject to the Kondo effect.

IV. CONCLUSIONS

Mo₄Ce₄Al₇C₃ is a particularly clear example of a FM Kondo lattice, as revealed by magnetotransport and ARPES experiments. Exploiting the element-specificity characteristic of XANES and XMCD gave us the key for deciphering the roles played by the two nonequivalent Ce sites. We evidenced

that the Ce2 sites embedded in the Al planes are in the $4f^1$ electronic configuration and are responsible for the ferromagnetism. In contrast, the Ce1 sites, pertaining to the Mo-C planes, are in a mixed valence state and the Ce1 atoms in the $4f^1$ configuration seem to show paramagnetic behavior. This is ascertained by the observation that neither Mo nor C atoms exhibit any discernible XMCD signal, whereas a substantial orbital magnetization exists on the Al atoms. The magnetism of the latter is obviously induced by their proximity with the ferromagnetically coupled Ce2 sites.

The FM interactions compete with Kondo interactions. Applying pressure leads the latter to progressively supersede the former. This is in line with the expected evolution of the two corresponding interactions' strengths with pressure. This is also consistent with the progressive increase of the $4f^0$ contribution and the concomitant increase in the number of conduction electrons with pressure, as highlighted by Ce L_3 XANES. Both magnetoresistance and specific-heat data, which are compatible with an effective $j = 1/2$ moment, confirm that crystal-field effects are important and result in the population of the lowest Kramers doublet of the split $4f$ level. Since the Ce1 sites are not FM, the existence of competing FM and Kondo interactions implies that the Ce2 sites participate in the Kondo regime, and thus that conduction electrons are also delocalized in the Al planes. This is confirmed by DFT + U and ARPES results. A remaining unknown is whether the Ce1 sites also participate in the Kondo regime.

ACKNOWLEDGMENTS

This work was financially supported by the Flag-ERA JTC 2017 project entitled "MORE-MXenes" and by ESRF and Université Grenoble-Alpes through the IDEX-ISP program "MORE-MAX." High-pressure XANES was measured at ESRF through Proposal No. HC-3567. ARPES and XMCD were measured at SOLEIL through Proposals No. 20190146 and No. 20190597, respectively. We are grateful to the technical support offered at DEIMOS, CASSIOPEE, ID12, and ID27 beamlines for smoothly running the experiments. We also acknowledge the financial support of the Cross-Disciplinary Program on Instrumentation and Detection of CEA, the French Alternative Energies and Atomic Energy Commission. T.I. acknowledges support from Grant-in-Aid for Scientific Research (C) (Grant No. 17K05495).

- [1] E. Bauer, *Adv. Phys.* **40**, 417 (1991).
- [2] D. M. Newns and N. Read, *Adv. Phys.* **36**, 799 (1987).
- [3] P. S. Riseborough and J. M. Lawrence, *Rep. Prog. Phys.* **79**, 084501 (2016).
- [4] P. Coleman, in *Fundamentals and Theory*, Handbook of Magnetism and Advanced Magnetic Materials Vol. 1, edited by H. Kronmüller and S. Parkin (Wiley, New York, 2007).
- [5] M. Vojta, *J. Low Temp. Phys.* **161**, 203 (2010).
- [6] P. Nozières, *Ann. Phys. (Paris, Fr.)* **10**, 19 (1985).
- [7] C. Lacroix and M. Cyrot, *Phys. Rev. B* **20**, 1969 (1979).
- [8] P. Fazekas and E. Müller-Hartmann, *Z. Phys. B: Condens. Matter* **85**, 285 (1991).
- [9] U. S. Kaluarachchi, V. Taufour, S. L. Bud'ko, and P. C. Canfield, *Phys. Rev. B* **97**, 045139 (2018).
- [10] J. Kondo, *Prog. Theor. Phys.* **32**, 37 (1964).
- [11] D. L. Cox and N. Grewe, *Z. Phys. B: Condens. Matter* **71**, 321 (1988).
- [12] B. Coqblin, M. D. Núñez-Regueiro, A. Theumann, J. R. Iglesias, and S. G. Magalhães, *Phil. Mag.* **86**, 2567 (2006).
- [13] N. Andrei, K. Furuya, and J. H. Lowenstein, *Rev. Mod. Phys.* **55**, 331 (1983).
- [14] D. Kaczorowski, A. V. Gribanov, S. F. Dunaev, and E. V. Marushina, *Intermetallics* **95**, 130 (2018).

- [15] V. H. Tran and Z. Bukowski, *J. Phys.: Condens. Matter* **26**, 255602 (2014).
- [16] P. Manfrinetti, S. K. Dhar, R. Kulkarni, and A. V. Morozkin, *Solid State Commun.* **135**, 444 (2005).
- [17] M. Inamdar, A. Thamizhavel, and S. K. Dhar, *J. Phys.: Condens. Matter* **26**, 326003 (2014).
- [18] W. Kittler, V. Fritsch, F. Weber, G. Fischer, D. Lamago, G. André, and H. V. Lohneysen, *Phys. Rev. B* **88**, 165123 (2013).
- [19] C. Krellner, N. S. Kini, E. M. Brüning, K. Koch, H. Rosner, M. Nicklas, M. Baenitz, and C. Geibel, *Phys. Rev. B* **76**, 104418 (2007).
- [20] B. Andraka and G. R. Stewart, *Phys. Rev. B* **49**, 12359 (1994).
- [21] V. H. Tran, J. C. Griveau, R. Eloirdi, and E. Colineau, *Phys. Rev. B* **89**, 054424 (2014).
- [22] Q. Tao, T. Ouisse, D. Pinek, O. Chaix-Pluchery, F. Wilhelm, A. Rogalev, C. Opagiste, L. Jouffret, A. Champagne, J.-C. Charlier, J. Lu, L. Hultman, M. W. Barsoum, and J. Rosen, *Phys. Rev. Materials* **2**, 114401 (2018).
- [23] A. Gkountaras, Y. Kim, J. Coraux, V. Bouchiat, S. Lisi, M. W. Barsoum, and T. Ouisse, *Small* **16**, 1905784 (2020).
- [24] M. W. Barsoum, *MAX Phases* (Wiley, Weinheim, 2013).
- [25] M. W. Barsoum, *Prog. Solid State Chem.* **28**, 201 (2000).
- [26] Q. Tao, J. Lu, M. Dahlgqvist, A. Mockute, S. Calder, A. Petruhins, R. Meshkian, O. Rivin, D. Potashnikov, E. Caspi, H. Shaked, A. Hoser, C. Opagiste, R.-M. Galera, R. Salikhov, U. Wiedwald, C. Ritter, A. R. Wildes, B. Johansson, L. Hultman *et al.*, *Chem. Mater.* **31**, 2476 (2019).
- [27] Q. Tao, M. Dahlgqvist, J. Lu, S. Kota, R. Meshkian, J. Halim, J. Palisaitis, L. Hultman, M. W. Barsoum, P. O. Persson, and J. Rosen, *Nat. Commun.* **8**, 14949 (2017).
- [28] T. Ouisse, E. Sarigiannidou, O. Chaix-Pluchery, H. Roussel, B. Doisneau, and D. Chaussende, *J. Cryst. Growth* **384**, 88 (2013).
- [29] L. Shi, T. Ouisse, E. Sarigiannidou, O. Chaix-Pluchery, H. Roussel, D. Chaussende, and B. Hackens, *Acta Mater.* **83**, 304 (2015).
- [30] L. Joly, E. Otero, F. Choueikani, F. Marteau, L. Chapuis, and P. Ohresser, *J. Synchrotron Radiat.* **21**, 502 (2014).
- [31] P. Ohresser, E. Otero, F. Choueikani, K. Chen, S. Stanescu, F. Deschamps, T. Moreno, F. Polack, B. Lagarde, J. P. Daguerre, F. Marteau, F. Scheurer, L. Joly, J. P. Kappler, B. Muller, O. Bunau, and P. Saintavit, *Rev. Sci. Instrum.* **85**, 013106 (2014).
- [32] A. Rogalev and F. Wilhelm, *Phys. Met. Metallogr.* **116**, 1285 (2015).
- [33] D. Braithwaite, W. Knafo, R. Settai, D. Aoki, S. Kurahashi, and J. Flouquet, *Rev. Sci. Instrum.* **87**, 023907 (2016).
- [34] T. Ito, D. Pinek, T. Fujita, M. Nakatake, S. I. Ideta, K. Tanaka, and T. Ouisse, *Phys. Rev. B* **96**, 195168 (2017).
- [35] P. Blaha, K. Schwarz, F. Tran, R. Laskowski, G. K. H. Madsen, and L. D. Marks, *J. Chem. Phys.* **152**, 074101 (2020).
- [36] J. P. Perdew, K. Burke, and M. Ernzerhof, *Phys. Rev. Lett.* **77**, 3865 (1996).
- [37] T. Jo and A. Kotani, *Phys. Rev. B* **38**, 830 (1988).
- [38] H. B. Vasili, B. Casals, R. Cicheler, F. Macià, J. Geshev, P. Gargiani, M. Valvidares, J. Herrero-Martin, E. Pellegrin, J. Fontcuberta, and G. Herranz, *Phys. Rev. B* **96**, 014433 (2017).
- [39] J. Ph. Schillé, F. Bertran, M. Finazzi, Ch. Brouder, J. P. Kappler, and G. Krill, *Phys. Rev. B* **50**, 2985 (1994).
- [40] T. Okane, Y. Takeda, H. Yamagami, A. Fujimori, Y. Matsumoto, N. Kimura, T. Komatsubara, and H. Aoki, *Phys. Rev. B* **86**, 125138 (2012).
- [41] D. A. E. Fonda, P. E. Colavita, and G. Vlaic, *J. Synchrotron Radiat.* **6**, 34 (1999).
- [42] D. Li, G. M. Bancroft, M. E. Fleet, X. H. Feng, and Y. Pan, *Am. Mineral.* **80**, 432 (1995).
- [43] A. B. Altman, C. Das Pemmaraju, S. Alayoglu, J. Arnold, C. H. Booth, A. Braun, C. E. Bunker, A. Herve, S. G. Minasian, D. Prendergast, D. K. Shuh, and T. Tylliszczak, *Inorg. Chem.* **56**, 5710 (2017).
- [44] F. M. F. de Groot, M. A. Arrio, Ph. Saintavit, Ch. Cartier, and C. T. Chen, *Solid State Commun.* **92**, 991 (1994).
- [45] M. Pompa, A. M. Flank, and P. Lagarde, J. C. Rife, I. Stekhin, M. Nakazawa, H. Ogasawara, and A. Kotani, *Phys. Rev. B* **56**, 2267 (1997).
- [46] M. Nakazawa, H. Ogasawara, A. Kotani, and P. Lagarde, *J. Phys. Soc. Jpn.* **67**, 323 (1998).
- [47] M. Taupin, J.-P. Sanchez, J.-P. Brison, D. Aoki, G. Lapertot, F. Wilhelm, and A. Rogalev, *Phys. Rev. B* **92**, 035124 (2015).
- [48] C. Antoniak, H. C. Herper, Y. N. Zhang, T. K. A. Warland, F. Stromberg, B. Krumme, C. Weis, K. Fauth, W. Keune, P. Entel, R. Q. Wu, J. Lindner, and H. Wende, *Phys. Rev. B* **85**, 214432 (2012).
- [49] J.-i. Igarashi and K. Hirai, *Phys. Rev. B* **50**, 17820 (1994).
- [50] G. Y. Guo, *J. Phys.: Condens. Matter* **8**, L747 (1996).
- [51] H. Ebert, *Rep. Prog. Phys.* **59**, 1665 (1996).
- [52] J. P. Rueff, R. M. Galéra, Ch. Giorgetti, E. Dartyge, Ch. Brouder, and M. Alouani, *Phys. Rev. B* **58**, 12271 (1998).
- [53] V. N. Antonov, B. N. Harmon, and A. N. Yaresko, *J. Phys.: Condens. Matter* **19**, 186222 (2007).
- [54] Y. Takeda, Y. Saitoh, T. Okane, H. Yamagami, T. D. Matsuda, E. Yamamoto, Y. Haga, and Y. Onuki, *Phys. Rev. B* **97**, 184414 (2018).
- [55] J. F. Morar, F. J. Himpsel, G. Hollinger, G. Hughes, and J. L. Jordan, *Phys. Rev. Lett.* **54**, 1960 (1985).
- [56] Y. K. Chang, H. H. Hsieh, W. F. Pong, M.-H. Tsai, F. Z. Chien, P. K. Tseng, L. C. Chen, T. Y. Wang, K. H. Chen, D. M. Bhusari, J. R. Yang, and S. T. Lin, *Phys. Rev. Lett.* **82**, 5377 (1999).
- [57] H. Mertins, S. Valencia, W. Gudat, P. Oppeneer, O. Zaharko, and H. Grimmer, *Europhys. Lett.* **66**, 743 (2004).
- [58] M. Weser, Y. Rehder, K. Horn, M. Sicot, M. Fonin, A. B. Preobrajenski, E. N. Voloshina, E. Goering, and Yu. S. Dedkov, *Appl. Phys. Lett.* **96**, 012504 (2010).
- [59] J. B. S. Mendes, O. Alves Santos, T. Chagas, R. Magalhães-Paniago, T. J. A. Mori, J. Holanda, L. M. Meireles, R. G. Lacerda, A. Azevedo, and S. M. Rezende, *Phys. Rev. B* **99**, 214446 (2019).
- [60] T. L. A. Tran, P. K. J. Wong, M. P. de Jong, W. G. van der Wiel, Y. Q. Zhan, and M. Fahlman, *Appl. Phys. Lett.* **98**, 222505 (2011).
- [61] T. Ouisse, L. Shi, B. A. Piot, B. Hackens, V. Mauchamp, and D. Chaussende, *Phys. Rev. B* **92**, 045133 (2015).
- [62] P. Schlottmann, *Z. Phys. B: Condens. Matter* **51**, 223 (1983).
- [63] B. Battlogg, D. J. Bishop, E. Bucher, B. Golding, A. P. Ramirez, Z. Fisk, J. L. Smith, and H. R. Ott, *J. Magn. Magn. Mater.* **63–64**, 441 (1987).
- [64] P. T. Coleridge, *J. Phys. F: Met. Phys.* **17**, L79 (1987).
- [65] U. Rauchschwalbe, F. Steglich, and H. Rietschel, *Physica B+C (Amsterdam)* **148**, 33 (1987).
- [66] G. Chajewski, M. Pasturel, and A. P. Pikul, *J. Alloys Compd.* **706**, 244 (2017).

- [67] K. Alami-Yadri and D. Jaccard, *Solid State Commun.* **100**, 385 (1996).
- [68] S. Doniach, *Physica B+C (Amsterdam)* **91**, 231 (1977).
- [69] D. Pinek, T. Ito, M. Ikemoto, K. Yaji, M. Nakatake, S. Shin, and T. Ouisse, *Phys. Rev. B* **100**, 075144 (2019).
- [70] D. Das and D. Kaczorowski, *J. Magn. Magn. Mater.* **471**, 315 (2019).
- [71] C. D. Bredl, *J. Magn. Magn. Mater.* **63–64**, 355 (1987).
- [72] D. Pinek, T. Ito, M. Ikemoto, M. Nakatake, and T. Ouisse, *Phys. Rev. B* **98**, 035120 (2018).
- [73] D. Pinek, T. Ito, K. Furuta, Y. Kim, M. Ikemoto, S.-I. Ideta, K. Tanaka, M. Nakatake, P. Le Fèvre, F. Bertrand, and T. Ouisse, *Phys. Rev. B* **102**, 075111 (2020).
- [74] S. Patil, A. Generalov, M. Güttler, P. Kushwaha, A. Chikina, K. Kummer, T. C. Rödel, A. F. Santander-Syro, N. Caroca-Canales, C. Geibel, S. Danzenbächer, Yu. Kucherenko, C. Laubschat, J. W. Allen, and D. V. Vyalikh, *Nat. Commun.* **7**, 11029 (2016).
- [75] E. Weschke, C. Laubschat, T. Simmons, M. Domke, O. Strebel, and G. Kaindl, *Phys. Rev. B* **44**, 8304 (1991).
- [76] S. I. Fujimori, *J. Phys.: Condens. Matter* **28**, 153002 (2016).